Delft University of Technology

Accelerator-Based Tests of Shielding Effectiveness of Different Materials and Multilayers using High-Energy Light and Heavy Ions

Giraudo, Martina; Schuy, Christoph; Weber, Uli; Rovituso, Marta; Santin, Giovanni; Norbury, John W.; Tracino, Emanuele; Menicucci, Alessandra; Bocchini, Luca; More Authors

Important note
To cite this publication, please use the final published version (if applicable).
Please check the document version above.

Accelerator-Based Tests of Shielding Effectiveness of Different Materials and Multilayers using High-Energy Light and Heavy Ions

Author(s): Martina Giraudo, Christoph Schuy, Uli Weber, Marta Rovituso, Giovanni Santin, John W. Norbury, Emanuele Tracino, Alessandra Menicucci, Luca Bocchini, Cesare Lobascio, Marco Durante Chiara La Tessa

Accelerator-Based Tests of Shielding Effectiveness of Different Materials and Multilayers using High-Energy Light and Heavy Ions

Martina Giraudo,[a,b] Christoph Schuy,[c] Uli Weber,[c] Marta Rovituso,[d] Giovanni Santin,[e] John W. Norbury,[f] Emanuele Tracino,[g] Alessandra Menicucci,[h] Luca Bocchini,[a,i] Cesare Lobascio,[a] Marco Durante[d] and Chiara La Tessa[d,j,1]

[a] *Thales Alenia Space, Turin, Italy;* [b] *Department of Applied Science and Technology, Politecnico di Torino, Italy;* [c] *GSI Helmholtz Center, Darmstadt, Germany;* [d] *Trento Institute for Fundamental Physics and Applications (TIFPA), National Institute for Nuclear Physics, (INFN), Povo, Italy;* [e] *European Space Agency, Noordwijk, Netherlands;* [f] *NASA Langley Research, Hampton, Virginia;* [g] *Alter Elettronica s.r.l., Casale Monferrato, Italy;* [h] *Delft University of Technology, Delft, Netherlands;* [i] *Department of Physics, University of Torino, Torino, Italy; and* [j] *Department of Physics, University of Trento, Povo, Italy*

Giraudo, M., Schuy, C., Weber, U., Rovituso, M., Santin, G., Norbury, J. W., Tracino, E., Menicucci, A., Bocchini, L., Lobascio, C., Durante, M. and La Tessa, C. Accelerator-Based Tests of Shielding Effectiveness of Different Materials and Multilayers using High-Energy Light and Heavy Ions. *Radiat. Res.* 190, 526–537 (2018).

The roadmap for space exploration foresees longer journeys and further excursions outside low-Earth orbit as well as the establishment of permanent outposts on other celestial bodies, such as the Moon or Mars. The design of spacecrafts and habitats depends heavily on the mission scenario and must consider the radiation protection properties of the structural components as well as dedicated shielding. In fact, short- and long-term effects caused by exposure to cosmic radiation are now considered among the main health risks of space travel. One of the current strategies is to find multifunctional materials that combine excellent mechanical properties with a high shielding effectiveness to minimize the overall load. In this work, the shielding effectiveness of a wide variety of single and multilayer materials of interest for different mission scenarios has been characterized. In the experimental campaign, reference and innovative materials, as well as simulants of Moon and Mars *in situ* resources, were irradiated with 1,000 MeV/u ^{4}He, 430 MeV/u ^{12}C and 962–972 MeV/u ^{56}Fe. The results are presented in terms of Bragg curves and dose reduction per unit area density. To isolate the shielding effectiveness only due to nuclear fragmentation, a correction for the energy loss in the material is also considered. These findings indicate that the best shield is lithium hydride, which performs even better than polyethylene. However, the technical feasibility of shielding needs to be investigated. The classification of all materials in terms of shielding effectiveness is not influenced by the ion species, but the value changes dramatically depending on the beam energy. The output of this investigation represents a useful database for benchmarking Monte Carlo and deterministic transport codes used for space radiation transport calculations. These findings also contribute to recommendations for optimizing the design of space vessels and habitats in different radiation environments. © 2018 by Radiation Research Society

[1] Address for correspondence: Department of Physics, University of Trento, Via Sommarive 14, 38123 Povo, Italy; email: chiara.latessa@unitn.it.

INTRODUCTION

Future human exploration into interplanetary space will expose astronaut crews to increased health hazards compared to the current low-Earth orbit (LEO) missions on the International Space Station (ISS). It is now generally acknowledged that exposure to space radiation represents the main health risk for exploration-class missions (*1*). In deep space, astronauts will be exposed to the full spectrum of galactic cosmic rays (GCR) and solar particle events (SPE) (*2*). The former consist of high-energy ions of galactic origin while the latter are particles (mainly protons) ejected from the Sun. The radiation hazard is further aggravated by the mission duration (*3*). Currently, a journey to Mars is estimated to last approximately 3 years, which is well above the average time spent in space so far. The combination of increased mission length with the radiation environment in deep space will result in radiation dose that exceeds the currently accepted limits (*4, 5*). As time in space will be increased, rather than decreased, according to the plans for exploration and colonization (*6*), some of the best tools for minimizing the risk to crew members are mission planning and spacecraft design. Shielding optimization plays a major role in this strategy. Among the solutions currently available, passive systems seem to be the only realistic option (*7*), as active shielding (*8, 9*) and biology-based countermeasures (*10*) are both still in a preliminary phase.

When designing a passive shield, it is important to consider that the amount of material required to completely stop GCRs or SPEs is impractical on current spacecraft. The feasibility of a mission depends heavily on the mass load

TABLE 1
List of All Single Materials Selected for this Study

Sample short name	Material description	Density (g cm^{-3})
Al	Pure aluminum	2.7
Al-2024	Aluminum alloy type 2024	2.694
Al-57-15	Aluminum honeycomb 57 (15°)	2.64
Al-60-15	Aluminum honeycomb 60 (15°)	2.64
Al-60-0	Aluminum honeycomb 57 (0°)	2.64
CFRP	Carbon fiber-reinforced plastic	1.5
DMK-M	Demokritos magnetized	1.073
DMK-N	Demokritos nonmagnetized	1.073
Epoxy	Epoxy	1.153
Epoxy + N	Epoxy with carbon nanotubes (HDPE filling)	1.153
HDPE	High-density polyethylene	0.97
Kevlar	Kevlar epoxy	1.1667
LiH	Lithium hydride	0.53
Moon C	DNA-1 Moon concrete	1.64
Moon S	ORBITEC JSC-1 Moon simulant	1.76
Mars S	ORBITEC JSC-1 Mars simulant	0.93
Nextel	Nextel	1.1429
PMMA	Lucite - poly(methyl methacrylate)	1.185
PPSU	Polyphenylsulfone	1.29

Note. The composition, density and name referred to in the article are specified.

and thus the current materials used as shielding are selected for their dose reduction capability per mass unit, and are also usually optimized for other purposes (*11*). On the other hand, once the mission destination has been reached, *in situ* resources can be used in large quantities to protect permanent habitats.

The ROSSINI project of the European Space Agency (ESA) is a ground-based study of shielding for space travel. Its approach is based on the use of single high-energy heavy-ion beam attenuation to estimate the shielding effectiveness of different materials (*12*). Results obtained by the Lawrence Berkeley Laboratory group showed that 1,000 MeV/u ^{56}Fe ions are a proxy of the heavy ion component of the GCR spectrum for these measurements (*13*). Taking advantage of the same technique, the properties of the structural materials Kevlar® and Nextel™ have been investigated in a previously published study (*14*). The results of the accelerator-based experiments using 1,000 MeV/u ^{56}Fe ions have been confirmed with exposures of Kevlar and Nextel on the ISS (*15, 16*), demonstrating that the former predict the radiation shielding of a given material or multilayer composite shield in space (*17*). All these findings cannot be easily applied to the proton component of the GCR, as they behave completely differently from heavy ions. A dedicated study for the optimization of shielding materials against these particles is currently underway and the results will be reported at a later date. The main goals of the ROSSINI study are:

1. Trade-off analysis of potential innovative shielding and multifunctional materials. The selection considers only candidates that fulfilled pre-screening criteria for their use in space applications (e.g., safety, low cost, light weight, strength, etc.) and also includes layered shielding structures.
2. Simulation of the radiation transport and secondary particle generation through the selected materials, using different Monte Carlo radiation transport codes, including GRAS/Geant4 (*18*) and PHITS (*19*).
3. Design and manufacturing of radiation shielding test samples.
4. Testing of the selected materials with high-energy ions simulating GCRs and SPEs.
5. Simulation of a realistic habitat and/or vehicle for human exploration beyond ISS.
6. Evaluation of radiation doses absorbed in human tissue, given the particle species and energy spectra observed inside the habitat/vehicle considered.

Results of the test campaigns conducted within the ROSSINI and ROSSINI 2 projects are reported and discussed in this article.

MATERIALS AND METHODS

Selection of Candidate Materials

The selection of candidate materials for this study was guided by the physics of particle interactions (electromagnetic and nuclear) and by their usability in spacecraft design. Different kinds of samples were considered: standard materials already used for structural and shielding purposes in space vehicles, innovative materials optimized for radiation protection applications, simulants of Moon and Mars soil and multilayer configurations to reproduce both hard and soft (inflatable) structures for deep-space or planetary mission scenarios.

It is clear that the electromagnetic energy loss and nuclear fragmentation counteract each other in a shield (*20*). The dose escalation caused by the linear energy transfer (LET) rise is an unwanted (but unavoidable) effect and competes with the dose attenuation stemming from the nuclear breakup of the incoming particles, which are broken up into lighter fragments of less biological significance. This consideration has encouraged the selection of shielding materials toward those with high-fragmentation capabilities, which yield a high dose reduction with a small thickness, thus minimizing energy loss processes. Additionally, the ideal shield produces no secondary neutrons, and thus lighter nuclei are preferable, as they have a lower breakup probability and contain fewer neutrons (e.g., hydrogen contains no neutrons while oxygen and carbon tend to disintegrate into helium nuclei without producing any neutron). Together with the estimated nuclear fragmentation probability per mass, the trade-off method for the selection of materials to be tested is based on the analytical hierarchy process (*21*), which also takes into account the following elements: safety, cost, availability and compatibility with thermal and mechanical mission environments. All materials selected for the study are listed in Table 1, and multilayer configurations are listed in Table 2.

Materials currently used in space. The shielding effectiveness of materials already employed in space has been measured. Two kinds of samples belong to this category: those with excellent mechanical properties used for building space vessel structures and those specifically selected as shields against radiation.

1. High-density polyethylene (HDPE), polymethyl methacrylate (PMMA), pure aluminum and aluminum alloy (AL-2024) have been included in the investigation as reference materials. Polyethylene is currently used as a shielding system on the ISS

TABLE 2
List of all Multilayer Configurations

Sample short name	Components and their area density (g cm⁻²)	Area density (g cm⁻²)
Light MDPS	Betha cloth (0.03)	0.56
	Nextel (0.3)	
	Kevlar epoxy (0.23)	
A	Al (0.675)	3.61
	Nextel (0.628)	
	Kevlar epoxy (0.933)	
	Light MDPS (0.56)	
	Al (0.81)	
B	Al (0.675)	3.25
	Nextel (0.628)	
	Kevlar epoxy (0.933)	
	Light MDPS (0.56)	
	CFRP (0.45)	
C	Light MDPS (0.56)	1.01
	CFRP (0.45)	
D	Light MDPS (0.56)	1.37
	Al (0.81)	
E	Aluminum 2024 (0.57)	1.97
	Kevlar Epoxy (0.7)	
	Nextel (0.4)	
	CFRP (0.3)	
E + LiH	Multilayer E	8.10
	Lithium hydride (6.14)	
E + H₂O	Multilayer E	6.97
	Water (5)	
F	Nextel (1.2)	1.23
	Inflatable Kevlar + bladder (0.028)	
F + LiH	Multilayer F	7.37
	Lithium hydride (6.14)	
F + H₂O	Multilayer F	6.23
	Water (5 cm)	
Moon S + F	Moon simulant (21.05)	22.28
	Multilayer F	
Moon S + F + LiH	Moon simulant (21.05)	28.42
	Multilayer F	
	Lithium hydride (6.14)	
Moon S + F + H₂O	Moon simulant (21.05)	27.28
	Multilayer F	
	Water (5)	
G	PU (polyurethane)-bladder/Kevlar composite (0.144), 4 layers	0.58
H	Aluminum 2024 (0.295)	1.84
	Nextel (0.4)	
	Kevlar (0.866)	
	CFRP (0.273)	
H + PPSU	Multilayer H	5.73
	PPSU (3.898)	
H + Moon S	Multilayer H	20.85
	Moon Simulant (19.015)	

Note. The composition, density and name referred to in the article are specified.

(22), while aluminum is the standard construction material for any spacecraft.

2. Honeycomb structures are used in the spacecraft structure to minimize the amount of material and, at the same time, to obtain acceptable out-of-plane compression and shear properties. Among the many shapes and features, two samples made of the aluminum alloy type 5056, and with different hexagonal cell sizes (referred to as Al-57 and Al-60) have been selected for this campaign. To assess how the periodicity influenced the shielding properties, both targets were measured; once with the holes parallel to the beam direction (Al-60-0°) and once tilted by 15° (Al-57-15° and Al-60-15°) with respect to the plane perpendicular to the beam direction.

3. Kevlar resin is composed of 18 layers of Kevlar fabric embedded in epoxy resin. As with Nextel fibers, this material is extensively used to protect the manned elements of the ISS against micrometeoroids and space debris (micrometeoroids and debris protection system; MDPS).

4. Due to its mechanical and chemical properties, polyphenylsulfone (PPSU) is a good candidate for building internal structures and, if properly treated, as window material.

Innovative materials. Novel materials were selected for their promising shielding capabilities and irradiated in all test campaigns.

These candidates can be used as radiation shields on either the spacecraft or as a component of habitat structures.

1. Mars and Moon simulants are in a dust form (not pressed) and were contained in either flasks of polystyrene or boxes made of Laminil™ (a sandwich of expanded polystyrene and cardboard). The area densities reported and used to calculate the shielding effectiveness include both the material and the container. Moon concrete is produced by mixing moon simulant with a chemical binder and shaped as tiles of area 10×10 cm^2 (23).
2. Lithium hydride (LiH) in compressed powder pellets has been selected as the most promising alternative to HDPE for its lower mass number (higher hydrogen content and exchange of carbon with lithium), reasonable chemical stability and limited toxicity. Once they are produced, the pellets are placed in thin PE bags, whose thickness has been considered in the overall target area density (as for the Mars/Moon simulants).
3. Among several epoxy-based nanocomposites, the carbon nanotubes Plasticyl™ HDPE 1501 at 3% filling concentration was selected for its high hydrogen content and best thermal properties (Epoxy + N). A sample without filler has also been tested as a reference (Epoxy).
4. Carbon fiber-reinforced plastic (CFRP) is an extremely strong and light plastic reinforced with carbon fibers which has been considered as the main component of the spacecraft primary structure as an alternative to Al-2024.
5. The target produced by Demokritos laboratories (referred to as DMK-M) is a multilayered tile consisting of 20 equidistant ultrathin (approximately 10 μm) slabs of nano- and micro-sized neodymium-iron-boron (Nd$_2$Fe$_{14}$B) magnetic particles (10% weight) with random magnetic orientation embedded in a HDPE matrix (24). The goal was to test whether the Lorentz forces exerted by the numerous micro-magnets on the traversing charged particles can be exploited to increase scattering probability and net absorption cross section compared to a non-magnetized sample (DMK-N).

Multilayers. Different types of multilayers have been included in this investigation, reproducing actual or alternative space vessel structures and as simulants of future planetary habitats.

1. Multilayer A reproduces a simplified configuration of the ISS Columbus pressurized module external shell, optimized to be a light MDPS and to guarantee a habitable inner volume.
2. Multilayer B is a hybrid configuration based on the actual Columbus structure and optimized for next-generation Earth space station structures.
3. Multilayers C and D are light MDPS plus a CFRP or an aluminum shell, respectively, and represent good candidates to be employed in future interplanetary missions.
4. Multilayers E and F reproduce a rigid simplified protection from the external environment (micrometeoroids and debris) and have been tested alone and in combination with LiH or water as dedicated shielding materials. Additionally, to simulate a lunar habitat, the measurements of a thick layer of Moon simulant have been added in front of the multilayer F.
5. Multilayer G is a composite of Kevlar and a polyurethane (PU) bladder (folded twice for a total of four layers, to reach a less noisy attenuation signal) and which could serve as a skin for an inflatable habitat, with the PU bladder maintaining the internal pressure.
6. Multilayer H is similar to Multilayer E, but with slightly different thicknesses.

Experimental Set up

The shielding effectiveness of all materials listed in Tables 1 and 2 has been assessed by measuring their performance in reducing the

TABLE 3
Beams Selected to Measure the Shielding Effectiveness of All Candidate Materials

Beam	Energy (MeV/u)	Range in water (cm)	Facility
^{4}He	1,000	324	NSRL
^{56}Fe	962	24.6	
	972	25	
^{12}C	430	30	HIT

dose when exposed to high-energy charged particles. The beams selected for the test campaign as proxy for the GCRs are listed in Table 3.

The experiments were performed at the NASA Space Radiation Laboratory (NSRL) (25) at Brookhaven National Laboratory and at the Heavy Ion Therapy (HIT) center (26). For the experiments performed at NSRL, all samples were exposed to a 20×20 cm^2 irradiation field and enough particles were delivered for each measurement to avoid statistical fluctuations. At HIT, the carbon pencil beam had a Gaussian profile with an 8-mm full width at half maximum (FWHM) and an intensity of 3×10^7 particles s^{-1}. In both setups, an ion chamber with an active area larger than the beam profile (40×40 cm^2 at NSRL and 20×20 cm^2 at HIT) was placed upstream of the material to monitor the incoming beam. At NSRL, the dose behind the shielding was measured with a proportional counter model IC-17A (produced by Far West Technology, Goleta, CA) placed as close as possible (less than 1 cm distance) to the target. At HIT, a build-up compensator slab (20 mm PMMA) and a second ionization chamber (20×20 cm^2 active area) were placed in-line and next to each other and downstream of the target, at a distance of 55 cm from the beam monitor chamber. The compensator plate mitigates the typical dose increase caused by the electron build-up, especially in the first mm of the target material (27) and reduces the sensitivity to the (relative) uncertainties of the thickness for thin targets. This improves the comparability between different target materials. A schematic of the experimental setups used in this investigation is shown in Fig. 1.

In both test campaigns, a no-target measurement was also acquired to provide the normalization factor from which the dose reduction could be calculated. The main difference between the two experimental approaches (NSRL and HIT) is the choice of both the downstream detector and beam profile size. The rationale behind the NSRL setup was to ensure that the downstream detector was fully immersed in the radiation field produced by the shield, as it is in space. Therefore, a large beam profile and a small proportional counter were selected. At HIT, the decision was made to use detectors with an active area much larger than the irradiation field to obtain a fully lateral integration of the beam spot, which is a standard methodology in ion therapy for precise Bragg curve measurements. HIT does not provide a broad scattered beam but only pencil beams for raster scanning.

Both experimental setups used at HIT and NSRL were optimized to characterize the dose contribution from charged particles and not from neutrons, whose interaction probability in either the proportional counter or the ion chambers is very low. The production of secondary neutrons has been measured in a dedicated test campaign within the project for several projectile-target systems and will be reported at a later date. Furthermore, if the energy of the secondary ions was too low to reach the detector's active area (as is often the case for target fragments), their contribution to the dose could not be scored.

Data Analysis

The simplest approach to assess the shielding effectiveness of a material is to measure the change in dose, also referred to as dose reduction:
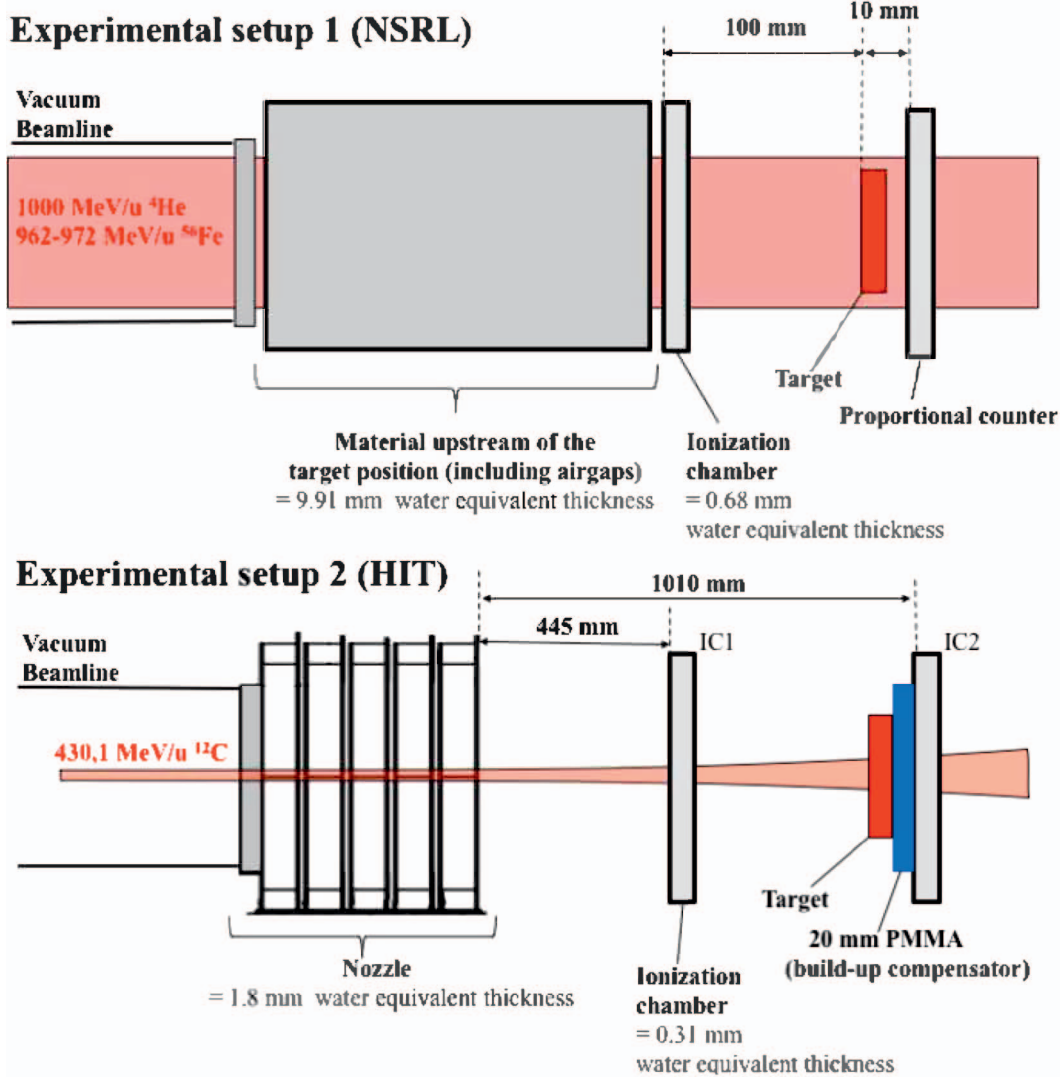
FIG. 1. Schematics of the experimental setups used for the test campaign at NSRL (upper) and HIT (lower).

$$\delta D = 1 - \frac{(D_{out}/D_{in})_T}{(D_{out}/D_{in})_0}, \qquad (1)$$

where D represents the doses recorded downstream (out) and upstream (in) of the shield. The values D_{out}/D_{in} indicated with subscript T were measured with the target and normalized by the no-target data (indicated with subscript 0). The latter considers the dose changes due to the experimental setup itself (detectors, air gaps, etc.). If plotted as a function of the material depth, D_{out}/D_{in} represents the Bragg curve. For the measurements performed at HIT the ratio $(D_{out}/D_{in})_0$ was always measured with the build-up slab.

Since targets of many thicknesses were used in this study, it is desirable to display the results in a manner that is depth independent. One approach is to divide Eq. (1) by the material thickness x and density ρ to obtain a normalized dose reduction δD_n with units of (g cm^{-2})$^{-1}$:

$$\delta D_n = \frac{\delta D}{x\rho} = \frac{1}{t}\left[1 - \frac{(D_{out}/D_{in})_T}{(D_{out}/D_{in})_0}\right], \qquad (2)$$

where t is the area density of the tested sample.

In previously published work, the trend of δD_n as function of the target thickness was found to be well described by a simple exponential function (13):

$$\delta D_n(t) = a\, exp[-tb], \qquad (3)$$

where the parameter, a, represents the extrapolated normalized dose reduction at zero (or infinitesimal) depth, also referred to as the shielding effectiveness of the material. This represents an alternative methodology to Eq. (1) when measured values are available for several target thicknesses. In principle, the exponential fit can also be performed on the initial part of the Bragg curve, where the primary beam LET remains almost unchanged. In this case the shielding effectiveness is equal to the parameter, b.

Energy Loss Correction

The dose decrease caused by nuclear fragmentation is mitigated by the LET dE/dx increase induced by the beam slow-down inside the material. This effect is smaller for high-energy beams (~1,000 MeV/u), where the energy loss in the plateau region of the curve is small and the LET is quasi-energy independent, but the effect becomes increasingly relevant as the target thickness increases or the beam initial energy is lower. To assess the shielding effectiveness originating only from the nuclear break-up of the particles, the results were corrected to allow for the beam dE/dx increase. This correction allows for a direct comparison of measurements obtained with

different beam species and energies, which otherwise would not be meaningful.

Using the LISE++ code (28), the theoretical energy loss of the primary ions in the downstream detector (det) is calculated with and without the energy change caused by the target. These two quantities are referred to as ΔE_T and ΔE_0, respectively, with the former being always higher than the latter. The ratio $(\Delta E_0/\Delta E_T)_{det}$ represents the correction factor and is applied to Eq. (2) to get an adjusted value of the normalized dose reduction δD_n:

$$\delta D_{n,corr} = \frac{1}{t}\left[1 - \frac{(D_{out}/D_{in})_T}{(D_{out}/D_{in})_0} \times \left(\frac{\Delta E_0}{\Delta E_T}\right)_{det}\right]. \qquad (4)$$

The shielding effectiveness of all materials has been calculated without and with this correction. The former reproduces a closer scenario to the actual one in space, where the dose delivered behind the shielding is the result of all occurring physical processes. The GCR spectrum peaks close to 1,000 MeV/u, and even at a lower energy for light-ion species. This was one of the motivations for conducting a dedicated test campaign with 430 MeV/u ^{12}C particles. For GCR radiation in the medium–high-energy range (400–1,000 MeV/u), the energy loss in a shielding of reasonable thickness will not be minimal. Thus, for these particles, fragmentation plays a major role in their interaction with the shielding and, as discussed above, has been exploited to mitigate the overall dose.

Error Analysis

A conservative error analysis was performed for the values δD_n and $\delta D_{n,corr}$. The uncertainty on the D_{out}/D_{in} values was assessed by repeating the measurements with a given target several times (typically 5) to obtain the mean value for D_{out}/D_{in} and its associated standard error. The same procedure was also done without the target to calculate an average dose reduction δD according to Eq. (1). The error in the δD_n values (and similarly in $\delta D_{n,corr}$) was then calculated using the following formula:

$$\Delta(\delta D_n) = \left(\frac{\Delta t}{t}\right)\frac{1}{t}\left[1 - \frac{\left(\frac{D_{out}}{D_{in}}\right)_T}{\left(\frac{D_{out}}{D_{in}}\right)_0}\right]$$

$$+ \frac{1}{t}\frac{\left(\frac{D_{out}}{D_{in}}\right)_T}{\left(\frac{D_{out}}{D_{in}}\right)_0}\left[\left(\frac{\Delta\left(\frac{D_{out}}{D_{in}}\right)_T}{\left(\frac{D_{out}}{D_{in}}\right)_T}\right)^2 + \left(\frac{\Delta\left(\frac{D_{out}}{D_{in}}\right)_0}{\left(\frac{D_{out}}{D_{in}}\right)_0}\right)^2\right]^{1/2}. \qquad (5)$$

The uncertainty in D_{out}/D_{in} for thin targets is much more relevant than for thick targets, because the second term of Eq. (5) becomes large for small area densities, t. Therefore, targets too thin (<0.2 g cm^{-2}) were excluded from he test series or were folded/stacked several times.

An additional source of error on the normalized dose reduction δD_n stems from the material structure itself, and the associated error Δt [first term of Eq. (5)] was quantified for each sample independently. The experimental thickness (measured dividing the target weight by area) was compared to the nominal value and the discrepancy averaged. The results vary between 0.5 and 4%, being the largest for the powders (Moon and Mars simulants and LiH) and for the Moon concrete.

RESULTS

^{56}Fe-Ion Beam

The partial or full Bragg curves for different target materials are plotted in Fig. 2, while the δD_n and $\delta D_{n,corr}$ values as a function of the target thickness in g cm^{-2} are shown in Fig. 3.
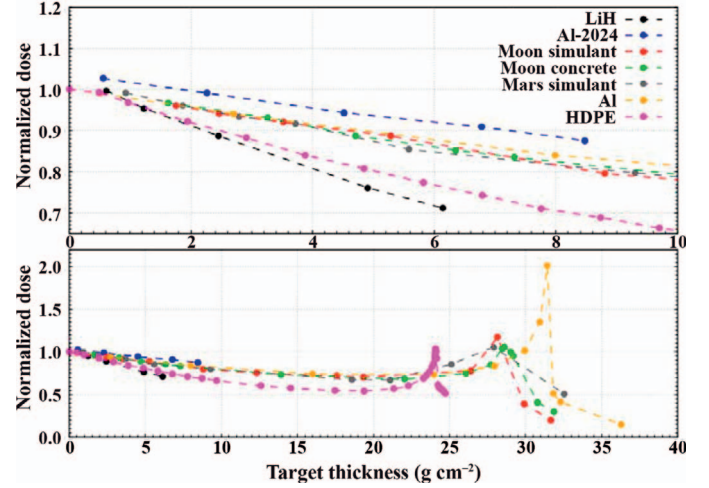

FIG. 2. Partial or full Bragg curves of 968 MeV/u ^{56}Fe ions in aluminum, high-density polyethylene (HDPE), Moon and Mars simulants and 972 MeV/u ^{56}Fe ions in aluminum 2024 (Al-2024), lithium hydride (LiH) and Moon concrete. The upper plot shows the datasets magnified up to a depth of 10 g cm^{-2}. The characteristics of all materials can be found in Table 1.

As discussed in the Data Analysis (above), both datasets can be used to calculate the shielding effectiveness. In this work, the results have been obtained from the δD_n (or $\delta D_{n,corr}$) curves, when available. The main rationale behind this choice is to consider the dose build-up shown by all profiles in Fig. 3 at small depths, but not clearly visible in the Bragg curves of Fig. 2. The fitting procedure according to Eq. (3) has been applied, excluding the values in the build-up region (typically below 3–5 g cm^{-2} depending on the material type). A comparison between the shielding
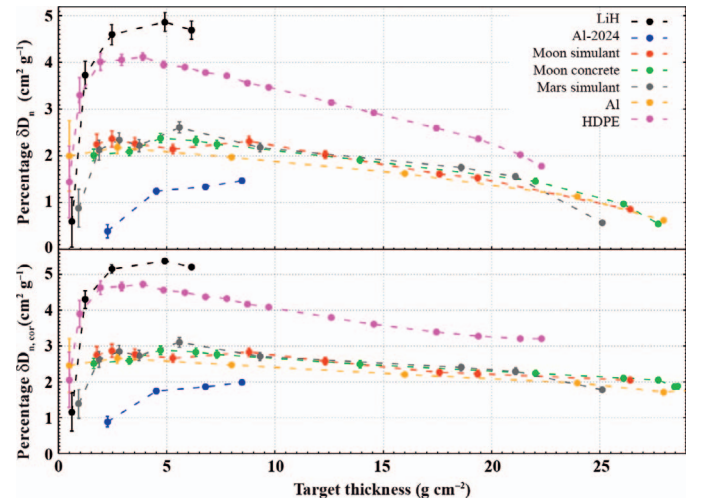

FIG. 3. Normalized dose reduction without (δD_n upper plot) and with ($\delta D_{n,corr}$ lower plot) the energy loss correction as a function of depth for aluminum (Al), high-density polyethylene (HDPE), Moon and Mars simulants irradiated with 968 MeV/u ^{56}Fe ions and Al-2024, LiH and Moon concrete irradiated with 972 MeV/u ^{56}Fe ions. Equations (2) and (4) have been used to calculate δD_n and $\delta D_{n,corr}$, respectively. The characteristics of all materials can be found in Table 1.
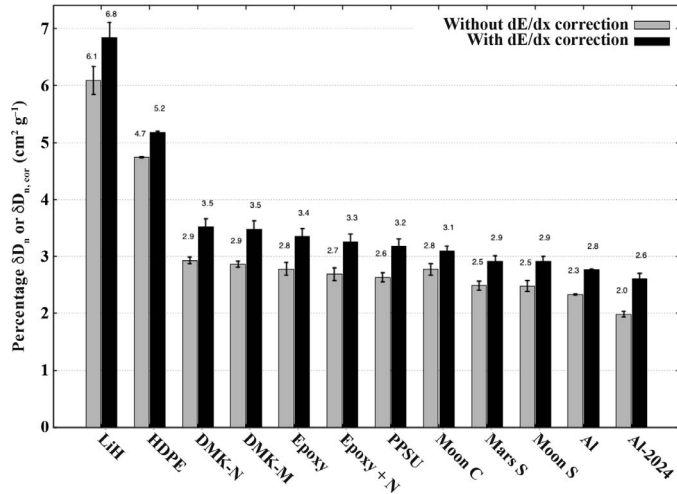
FIG. 4. Normalized dose reduction without (black) and with (red) the energy loss correction of Al, HDPE, Moon S and Mars S irradiated with 968 MeV/u ^{56}Fe ions and LiH, DMK-N, DMK-M, epoxy, epoxy + N, PPSU and Al-2024 exposed to 972 MeV/u ^{56}Fe ions. The characteristics of all materials are shown in Table 1. The exact dose reduction values are reported in percentage on top of each column.

effectiveness calculated from the Bragg curves and from the normalized dose reduction curves indicates that the results are close to, but not within the error, the former being always lower than the latter. The results for all single materials are plotted in Fig. 4. For those samples where only one thickness was available, Eqs. (2) and (4) have been used instead of the fitting procedure. Values for lithium hydride and aluminum 2024 have been obtained by fitting the dose reduction δD (without and with the energy loss correction) measured at several depths with a simple exponential function, because of the lack of material available to collect data also outside the build-up region. The dose values measured behind the multilayer samples (Table 2) have not been normalized to their area density, as the goal of the study was to test them in specific configurations rather than to obtain their shielding effectiveness at zero depth. Following the same rationale, the energy loss correction was not applied to the data. The results are plotted in Fig. 5.

^{12}C-Ion Beam

The δD_n and $\delta D_{n,corr}$ values as a function of the target depth are plotted in Fig. 6 for those materials where more than two thicknesses were available. Their shielding effectiveness has been estimated from these curves by applying the fitting method, but all data points have been included because the compensator plate cancelled the build-up effect.

The shielding effectiveness of all single materials tested (including the samples shown in Fig. 6) is plotted in Fig. 7. If only one or two target thicknesses were available, the result was calculated as a simple mean value of Eqs. (2) or (4), the latter applied to consider the energy loss correction. The honeycomb aluminum targets (Al-57-15°, Al-60-15°
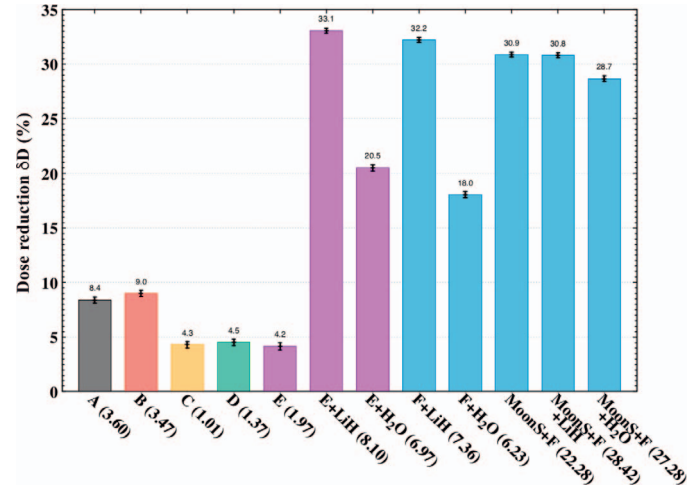

FIG. 5. Dose reduction of multilayer configurations exposed to 968 (samples A, B, C and D) or 972 MeV/u (samples E and F) ^{56}Fe ions. The characteristics of all samples are shown in Table 2. The target thicknesses in g cm^{-2} are reported in parentheses while the exact δD values are indicated in percentage on top of each column.

and Al-57-0°) are shown in a separate group because they have a specific structure. The shielding effectiveness of all multilayer configurations has been estimated with Eq. (1) and is shown in Table 4.

^{4}He-Ion Beam

The measurements of the full Bragg curves for the 1,000-MeV/u ^{4}He beam could not be performed due to the lack of material depth to match the ion's range. The normalized dose reduction δD_n as a function of the target thickness is plotted in Fig. 8.

For all samples exposed to this beam, the energy lost by the primary particles when traversing the target thickness is
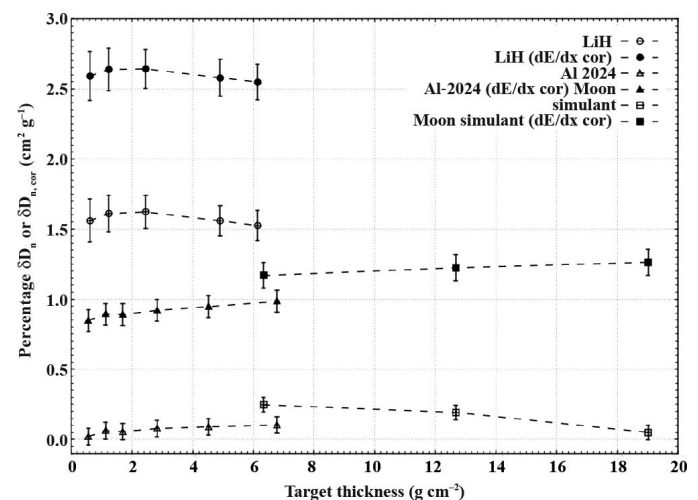

FIG. 6. Normalized dose reduction without (open symbols) and with (solid symbols) the energy loss correction as function of thickness for single shielding materials exposed to 430 MeV/u ^{12}C ions. The characteristics of all materials are shown in Table 1.
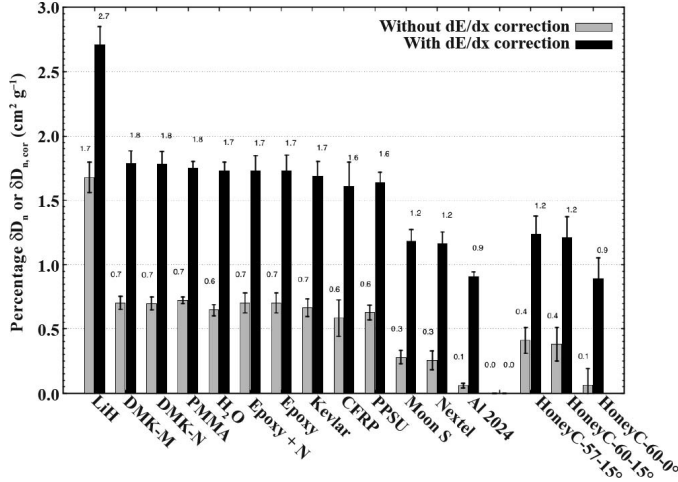
FIG. 7. Normalized dose reduction values for single shielding materials exposed to 430 MeV/u ^{12}C ions. The data are shown without (black) and with (red) the energy loss correction. The exact values are reported in percentage on top of each column. The characteristics of all materials are shown in Table 1.
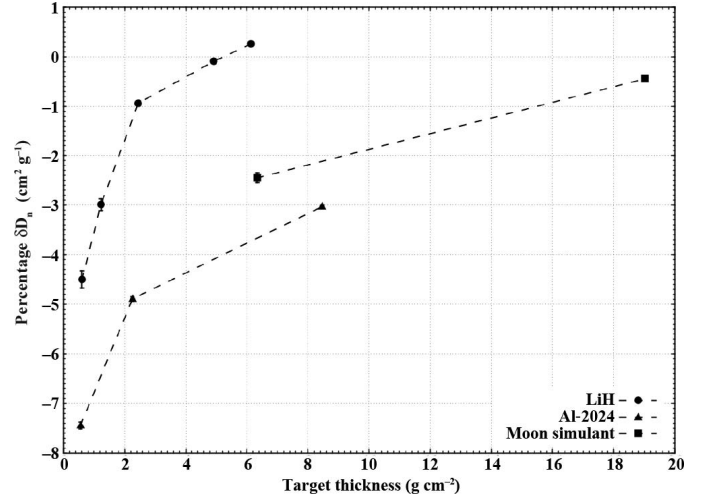

FIG. 8. Normalized dose reduction δD_n as a function of depth for several material types exposed to 1,000 MeV/u ^{4}He ions. The values were calculated using Eq. (2). The characteristics of all materials are shown in Table 1.

negligible (typically 0.2%), and thus no correction has been applied to the results.

The data collected with the ^{4}He beam could not be used to estimate a shielding effectiveness. Figure 8 indicates that the targets were not thick enough to yield a full δD_n curve, unlike the case for the ^{56}Fe (Fig. 3) and ^{12}C (Fig. 6) beams. Therefore, the results for single material types are presented as dose reduction δD (Fig. 9), as for the multilayer stacks (Table 5). A negative δD value means that the dose measured behind the target is higher than the dose delivered by the unshielded beam. In this case the sample cannot be considered a shield.

DISCUSSION

Elemental Targets: Heavy Ions

The Bragg curves measured with iron particles (Fig. 2) give a general indication of the target radiation protection properties (12, 13, 29). Pure aluminum, all simulants and the Moon concrete have a very similar trend in the plateau region, with values close to each other at a given depth. The dose measured in HDPE and LiH falls lower and faster than for the other materials, while Al-2024 is always above all others. The minimum dose before the Bragg peak is observed for HDPE, while the highest is for Al-2024. The

slope characteristics of LiH suggest that with this material the dose could be attenuated even more than with HDPE. The Bragg peak is found first in HDPE, then in all simulants (including the Moon concrete), and finally in aluminum at a much higher area density, following the increasing electron density of the materials (relative to the mass density). Additionally, the peak height is significantly higher than 1 only for aluminum. The Bragg curve shape is the result of the interplay between energy loss and nuclear fragmentation (20, 30). For a ^{56}Fe beam at approximately 1,000 MeV/u, nuclear processes dominate: primary ions undergo fragmentation while penetrating the shielding and are substituted by lighter particles with similar kinetic energy and thus lower LET. In the plateau region, this defines the curve slope: the more effective the material is in fragmenting

TABLE 4
Dose Reduction of Multilayer Configurations
Exposed to 430 MeV/u ^{12}C Ions

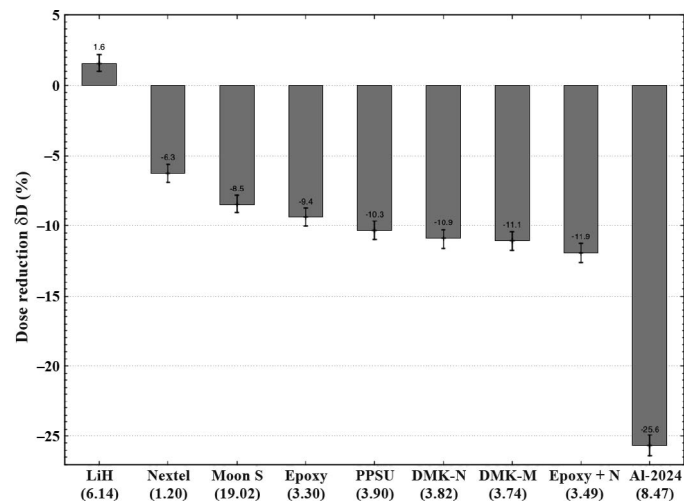| Multilayer	Thickness (g cm^{-2})	δD (%)
G	0.58	0.34 ± 0.03
H	1.84	0.91 ± 0.03
H + PPSU	5.73	3.34 ± 0.03
H + Moon S	20.85	0.03 ± 0.03

FIG. 9. Dose reduction of single materials exposed to 1,000 MeV/u ^{4}He ions. The target thicknesses in g cm^{-2} are reported in parentheses while the exact δD values are indicated in percentage on top of each column. The characteristics of all materials are shown in Table 1.

TABLE 5
Dose Reduction of Multilayer Configurations
Exposed to 1,000 MeV/u ^{4}He Ions

Multilayer	Thickness (g cm^{-2})	δD (%)
E	1.97	–5.7 ± 0.6
E + LiH	8.10	3.1 ± 0.6
E + H$_2$O	6.97	–13.1 ± 0.7
F + H$_2$O	6.23	14.6 ± 0.7
Moon S + F	22.28	3.0 ± 0.6
Moon S + F + LiH	28.42	19.6 ± 0.5
Moon S + F + H$_2$O	27.28	1.0 ± 0.6

TABLE 6
Total Fragmentation Cross Sections Available in the
Literature for ~1,000 MeV/u ^{56}Fe

Energy (MeV/u)	Ref.	σ$_{tf}$ (mb)		
		C	CH$_2$	Al
1,000	(12)	1537 ± 15	2859 ± 48	2010 ± 50
810	(31)	1626 ± 11	2968 ± 16	
1,050	(32)	1607 ± 10	3013 ± 16	

Note. The values for CH$_2$ (single molecule of polyethylene) from (12) were obtained by combining the data for C and H targets.

versus slowing down, the more pronounced is the dose fall off. The Bragg peak height represents another indicator of the role played by nuclear breakup. As the curves are normalized to the no-target value, a dose above 1 means that the material is causing a dose increase rather than decrease, and thus is not acting as a shield.

These results can be better interpreted taking advantage of the study from La Tessa *et al.* (29), which focused on the interaction of 1,000 MeV/u iron particles with thick metallic and plastic targets (>20 g cm^{-2}, i.e. close to the Bragg peak position). Their results showed that the average LET (<LET>$_{event}$) is highest for the no-target beam and is reduced by 30% with aluminum and by 50% with PMMA. The data also demonstrated that close to 70% of the primary ions impinging on the aluminum target do not undergo nuclear fragmentation up to the stopping region (while only 30% survive in PMMA). The limited fragmentation power of aluminum, combined with a small average LET decrease, caused the dose at the Bragg peak to be higher than at the target entrance, as also observed here. The same reasoning can be applied to all targets to understand their behavior.

A more direct way of assessing and comparing the shielding effectiveness of the materials is shown in Fig. 3, where the normalized dose reduction is plotted without and with the energy loss correction (^{56}Fe-Ion Beam subsection in Results.) as a function of target depth. All curves show a rapid rise (build-up) in the first few g cm^{-2}, reaching a maximum value, and then begin a slow drop with increasing thickness. The difference in behavior between low- and high-A (mass number) targets can be appreciated more clearly than in the Bragg curves. When the energy loss correction is applied (Fig. 3, bottom plot) the δD$_n$ fall-off at increasing target thickness becomes much smoother for all targets, but keeps showing a different trend for low- versus high-A targets, as for the uncorrected data. The correction increases the shielding effectiveness up to 20–40% of its initial value.

Other information that can help predict the shielding power of a material is the total fragmentation cross section σ$_{tf}$. Values available from the literature and of interest for this study are reported in Table 6.

The ratio σ$_{tf}$/A (i.e., the number of nuclear interactions per unit of mass) is highest for CH$_2$ (the single molecule of PE) and lowest for Al. This trend is directly translated into

an indication of the shielding characteristics of each material, as the slow-down due to electromagnetic interactions is very small at these energies. A detailed investigation of PE shielding properties when exposed to different ion-energy combinations can be found in Guetersloh *et al.* (33).

Data shown in Figs. 2 and 3 were used to extrapolate the shielding effectiveness at zero (or infinitesimal) depth. The results (Fig. 4) lead to the following conclusions:

1. LiH is the best shield against ~1,000 MeV/u iron ions, performing even better than HDPE (the current reference shielding material).
2. The magnetization of the Demokritos sample does not improve its shielding effectiveness.
3. Epoxy shows the same behavior without and with nanotubes.
4. All *in situ* resources have a similar δD$_{n,corr}$ of approximately 3% cm^2 g^{-1}.

The δD$_n$ values measured for aluminum and HDPE without the energy correction are not significantly different from previously reported measurements performed at Brookhaven National Laboratory (12–14, 17, 33–35). Given that the experimental methodologies are quite different, this result supports the reproducibility and consistency of the data.

It is important to note that the characterization of a material as a candidate shield against space radiation cannot be obtained from a single exposure, because its performance might depend on the ion species and energy. Nevertheless, Guetersloh *et al.* (33) showed that δD$_n$ values are nearly independent of the particle type for Z > 8 and at energies above ~600 MeV/u. Thus, the results obtained with the ^{56}Fe beam in this work can be considered as representative of a large part of the GCR heavy ion component.

Elemental Targets: Light Ions

Data collected with 430 MeV/u carbon (Figs. 6 and 7) and 1,000 MeV/u helium (Figs. 8 and 9) ions provide an indication of the material behavior with lighter particles.

A collection of total fragmentation cross sections found in the literature for carbon and of interest for this study are provided in Table 7.

The ratio σ$_{tf}$/A follows the same trend as iron, being highest for CH$_2$ and lowest for Al. However, the rather flat

TABLE 7
Total Fragmentation Cross Sections Available in the Literature for ~430 MeV/u ^{12}C

Energy (MeV/u)	Ref.	C	CH$_2$	Al
			σ_{tf} (mb)	
498	(36)	758 ± 15	1135 ± 15	1103 ± 28
400	(37)	713 ± 36	1011 ± 56	1033 ± 38
418	(32)	670 ± 7	1035 ± 10	
500	(38)	703 ± 17	1120 ± 78	1095 ± 27

Note. The values for CH$_2$ (single molecule of polyethylene) from (37) were obtained by combining the data for C and H targets.

plateau between the entrance channel and the Bragg peak region shown by carbon at this energy (20) indicates that nuclear fragmentation on the overall dose deposition is compensated by the energy loss processes. For this reason, the shielding effectiveness is, for instance, almost 0 for aluminum without the dE/dx correction and increases significantly from its initial value when the correction is applied (Figs. 6 and 7).

Published data reported in Tables 6 and 7 indicate that iron undergoes nuclear breakup between two and three times more than carbon depending on the material. The main consequence of the smaller fragmentation probability for 430 MeV/u carbon (and in general for light ions) compared to iron is that the overall shielding power of all materials is decreased.

All samples exposed to the helium beam caused a dose increase instead of a reduction, with the exception of LiH (Figs. 8 and 9), and started acting as a shield only above a certain thickness, whose value depends on the material type. A possible source of this finding is the build-up of forward-directed target fragments, which dominate the overall energy deposition and cover the effects of the primary ion's attenuation. For light ions like protons and helium, the nuclear build-up of target fragments has a clear effect on the depth-dose profile (39, 40). The higher the energy the more pronounced is the build-up in the entrance region (41). This hypothesis has been verified with Monte Carlo simulations for primary beams with energies of approximately 1,000 MeV/u and will be reported on in the future. For LiH, δD_n becomes positive at approximately 6 g cm^{-2}, while for the Moon simulant and Al-2024 the change occurs above 20 g cm^{-2}.

The lack of total fragmentation cross-section measurements for high-energy helium prevents the comparison between materials that was done for carbon and iron. The collection of data reported by Rovituso and La Tessa (20) indicates that the reaction cross section of ^{4}He and ^{12}C interacting with an ^{16}O target at energies close to those selected in this work is approximately 500 and 1,400 mb, respectively. The same trend is observed comparing values shown in Table 7 with cross sections for ^{4}He + ^{12}C collisions measured at HIT (40). These results indicate that helium fragments considerably less than carbon (and consequently iron) and therefore, even when the energy

loss is negligible, the protection offered by a given shielding is less effective against the helium component of the GCR.

Multilayer Materials

When the two configurations reproducing the Columbus hull (Fig. 5, multilayers A and B) were exposed to iron, they showed a similar shielding effectiveness, with a small increase when the inner layer of aluminum was substituted with CFRP. The dose reduction measured with the standard Columbus configuration (Fig. 5, multilayer A) agrees within the uncertainties with both experimental and Monte Carlo simulated values reported by Silvestri *et al.* (17). No significant differences were observed between alternative candidates that are to be employed as base structures for interplanetary mission vessels (Fig. 5, multilayers C and D).

For both simulants of a planet inflatable base (Fig. 5, multilayers E and F), the addition of LiH caused a much stronger dose decrease than water at comparable area density. This result reflects the trend of Fig. 4, where LiH proved to be a better shielding material than all other materials, including HDPE. To test the radiation protection performance of a possible permanent habitat, a thick layer of Moon simulant (~12 g cm^{-2}) was added to an inflatable base (Fig. 5, multilayer F). Its presence dominates the dose attenuation, which did not change when an extra layer of LiH or water (~5 g cm^{-2}) was included. A detailed study of the interaction between 1,037 MeV/u iron and sample materials in use on the ISS for the hull and the crew quarter interior walls were reported by Miller *et al.* (34).

Considering the different area density, multilayer G (inflatable habitat) has a superior shielding capability compared to multilayer H (possible hull for deep space mission vessel) when exposed to 430 MeV/u ^{12}C (Table 4). Adding the PPSU to multilayer H increased its shielding effectiveness from ~1% to 3%, while a thick layer of Moon simulant (19 g cm^{-2}) causes it to drop to 0. In the latter case, the total target thickness is close to the beam-stopping depth, where the steep LET increase dominates over nuclear fragmentation.

Multilayers exposed to 1,000 MeV/u ^{4}He showed different behaviors depending on the composition and thickness (Table 5), as already observed for single materials (Fig. 9). Figure 8 suggests that in the thickness range used for the tests, only LiH was able to yield a dose reduction instead of an increase. This is a direct consequence of the target fragment build-up already discussed for the single material results. At a comparable area density, adding LiH to multilayer E caused a dose decrease, while water had the opposite effect. The combination of multilayer F plus 12 g cm^{-2} of Moon simulant started acting as shielding (~3% dose reduction) and was boosted (~20%) with the addition of LiH.

Further ground-based test campaigns should take advantage of the GCR simulator available at the NSRL facility, which can reproduce a multi-ion and variable-energy

radiation field modeled on the actual GCR spectrum (*42*). The combination of the GCR and SPE simulators both available at NSRL provides the most advanced tool for studying the shielding effectiveness of single and multilayer materials, because the performance of each candidate material can be tested directly under realistic conditions. In this case, the shielding rank can be obtained simultaneously for all ions and energies, considering both fragmentation and energy loss contributions.

CONCLUSIONS

Here we report on an extensive study of the radiation protection properties of single and multilayer samples, which was performed within the ESA funded project ROSSINI. The test campaign included target materials currently used in different mission scenarios for structural or shielding functions as well as promising alternative candidates. The main rationale behind the selection was to find multifunctional materials that represent an optimal compromise between mechanical properties and radiation protection performance. Simulants of *in situ* resources were also studied because they are considered the best option for building permanent habitats on other planets. The output of this investigation can provide basic data for guidelines and recommendations for the design of space vessels, inflatable habitats and permanent outposts in different space environments. Additionally, the results represent a rich dataset for benchmarking Monte Carlo and deterministic codes currently used for space applications.

All experimental data presented here have been simulated with the GRAS (*18*) and PHITS (*19*) Monte Carlo transport codes, and those findings will be reported in the future. In most published studies, shielding properties have been measured by exposing the targets to $\sim$1,000 MeV/u ^{56}Fe ions, identified as representative of the high-charge and energy component of the GCR. However, the results of the Lawrence Berkeley Laboratory group (*33*) showed that the shielding effectiveness of a given material changes dramatically depending on the beam species and energy to which it is exposed. For example, 2.38 g cm^{-2} of PE exposed to 1,000 MeV/u ions of different species provided anywhere from a 5% dose reduction per g cm^{-2} to an increase of 1.1%. The influence of a shielding material, on both the delivered dose and the radiation field quality, results from the interplay of nuclear (breakup) and electromagnetic (energy loss) interactions. Due to the infeasibility of transporting into space a shield thick enough to fully stop the entire radiation spectrum, nuclear fragmentation is the most advantageous option for decreasing the dose. A recent overview of all fragmentation cross section measurements available in the literature (*43, 44*) pointed to significant gaps in the nuclear database, especially for light ions such as helium. Thus, existing measurements and Monte Carlo simulations alone are not enough to study the shielding effectiveness of all potential single- and multilayer materials when exposed to the full space radiation environment. A dedicated study like the current one provides a characterization of shielding materials in terms of their effectiveness in fragmenting the primary radiation, and by repeating the measurements with different particle species and energies, offers a more comprehensive picture.

The results from the test campaign showed that when the materials are ranked according to their shielding effectiveness only due to nuclear fragmentation (i.e., excluding the energy loss contribution), the ranking is the same for all ion species. Overall, LiH provides the highest dose reduction per g cm^{-2} (0.25% for helium, 2.11% for carbon and 6.84% for iron) performing even better than HDPE.

These findings suggest possible shielding strategies for medium-to-high-energy heavy ions, but they will have to be combined with additional data to give an overall recommendation. For instance, the production of secondary neutrons as well as target fragments are two important aspects that have not been considered here and will require a separate test campaign. The former have been recently studied in an extensive measurement campaign (*45, 46*) funded by NASA whose data are under analysis, while the characterization of target fragments is the aim of the ongoing experiment, Fragmentation of Target (FOOT; https://web.infn.it/f00t/index.php/en/) supported by INFN. Furthermore, the overall strategy will have to include a dedicated shielding approach for protons, which cannot be based on projectile fragmentation.

REFERENCES

1. Chancellor J, Scott G, Sutton J. Space Radiation: The Number one risk to astronaut health beyond low Earth orbit. Life 2014; 4:491–510.

2. Durante M, Cucinotta FA. Physical basis of radiation protection in space travel. Rev Mod Phys 2011; 83:1245–81.

3. Durante M, Bruno C. Impact of rocket propulsion technology on the radiation risk in missions to Mars. Eur Phys J D 2010; 60:215–218.

4. McKenna-Lawlor S, Bhardwaj A, Ferrari F, Kuznetsov N, Lal AK, Li Y, et al. Feasibility study of astronaut standardized career dose limits in LEO and the outlook for BLEO. Acta Astro 2014; 104:565–73.

5. Cucinotta FA, Kim MY, Chappell LJ, Huff JL. How safe is safe enough? Radiation risk for a human mission to Mars. PLoS One 2013; 8:e74988.

6. ISECG. The Global exploration roadmap. NP-2013-06. Washington, DC: NASA; 2013.

7. Durante M. Space radiation protection: Destination Mars. Life Sci Space Res 2014; 1:2–9.

8. Washburn SA, Blattnig SR, Singleterry RC, Westover SC. Active magnetic radiation shielding system analysis and key technologies. Life Sci Space Res 2015; 4:22–34.

9. Vuolo M, Giraudo M, Musenich R, Calvelli V, Ambroglini F, Burger WJ, et al. Monte Carlo simulations for the space radiation superconducting shield project (SR2S). Life Sci Space Res 2016; 8:22–9.

10. Kennedy AR. Biological effects of space radiation and development of effective countermeasures. Life Sci Space Res 2014; 1:10–43.

11. National Research Council. Managing Space Radiation risk in the Era of Space Exploration. Washington, DC: National Academy Press; 2008. Recommendation 5–7:87.

12. Zeitlin C, Guetersloh SB, Heilbronn LH, Miller J. Shielding experiments with high energy heavy ions for spaceflight applications. New J Phys 2008; 10:75007.

13. Zeitlin C, Guetersloh SB, Heilbronn LH, Miller J. Measurements of materials shielding properties with 1 GeV/nuc 56Fe. Nucl Instr Meth B 2006; 252:308–18.

14. Lobascio C, Briccarello M, Destefanis R, Faraud M, Gialanella G, Grossi G, et al. Accelerator-based tests of radiation shielding properties of materials used in human space infrastructures. Health Phys 2008; 94:242–7.

15. Pugliese M, Bengin V, Casolino M, Roca V, Zanini A, Durante M. Tests of shielding effectiveness of Kevlar and Nextel onboard the International Space Station and the Foton-M3 capsule. Radiat Environ Biophys 2010; 49:359–63.

16. Narici L, Casolino M, Di Fino L, Larosa M, Picozza P, Rizzo A, et al. Performance of Kevlar and Polyethylene as radiation shielding on-board the International Space Station in high latitude radiation environment. Sci Rep 2017; 7:1644.

17. Silvestri M, Tracino E, Briccarello M, Belluco M, Destefanis R, Lobascio C, et al. Impact of spacecraft shell composition on dose reduction. IEEE Trans Nucl Sci 2011; 58:3126–33.

18. Agostinelli S, Allison J, Amako K, Apostolakis J, Araujo H, Arce P, et al. Geant4 - a simulation toolkit. Nucl Instr Meth A 2003; 506:250–303.

19. Sato T, Niita K, Matsuda N, Hashimoto S, Iwamoto Y, Noda S, et al. Particle and heavy ion transport code system, PHITS, version 2.52. J Nucl Sci Technol 2013; 50:913–93.

20. Rovituso M, La Tessa C. Nuclear interactions of new ions in cancer therapy: impact on dosimetry. Transl Cancer Res 2017; 6:S914–33.

21. Saaty TL. Decision making with the analytic hierarchy process. Int. J Serv Sci 2008; 1:83.

22. Shavers MR, Zapp N, Barber RE, Wilson JW, Qualls G, Toupes L, et al. Implementation of ALARA radiation protection on the ISS through Polyethylene shielding augmentation of the service module crew quarters. Adv Space Res 2004; 34:1333–7.

23. Cesaretti G, Dini E, De Kestelier X, Colla V, Pambaguian L. Building components for an outpost on the lunar soil by means of a novel 3D printing technology. Acta Astro 2014; 93:430–50.

24. Kovacs A, Fischbacher J, Oezelt H, Schrefl T, Kaidatzis A, Salikhov R, et al. Micromagnetic simulations for coercivity improvement through nano-structuring of rare-Earth-free L1 0 - FeNi magnets. IEEE Trans Magn 2017; 53:1–5.

25. La Tessa C, Sivertz M, Chiang IH, Lowenstein D, Rusek A. Overview of the NASA space radiation laboratory. Life Sci Space Res 2016; 11:18–23.

26. Combs SE, Jakel O, Haberer T, Debus J. Particle therapy at the Heidelberg Ion Therapy Center (HIT) - Integrated research-driven university-hospital-based radiation oncology service in Heidelberg, Germany. Radiother Oncol 2010; 95:41–4.

27. Carlsson C. Proton dosimetry with 185 MeV protons. Dose buildup from secondary protons and recoil electrons. Health Phys 1977; 33:481–4.

28. Kuchera MP, Tarasov OB, Bazin D, Sherril B, Tarasova KV. LISE++ software updates and future plans. J Phys 2015; 664:072029.

29. La Tessa C, Guetersloh S, Heilbronn L, Miller J, Sihver L, Zeitlin C. Fragmentation of 1GeV/nucleon iron ions in thick targets relevant for space exploration. Adv Space Res 2005; 35:223–9.

30. Zeitlin C, La Tessa C. The role of nuclear fragmentation in particle therapy and space radiation protection. Front Oncol 2016; 6:65.

31. Ferrando P, Webber WR, Goret P, Kish JC, Schrier DA, Soutoul A, et al. Measurement of (12)C, (16)O, and (56)Fe charge changing cross sections in helium at high energy, comparison with cross sections in hydrogen, and application to cosmic-ray propagation. Phys Rev C 1988; 37:1490–1501.

32. Webber WR, Kish JC, Schrier DA. Total charge and mass changing cross sections of relativistic nuclei in hydrogen, helium, and carbon targets. Phys Rev C 1990; 41:520–32.

33. Guetersloh S, Zeitlin C, Heilbronn L, Miller J, Komiyama T, Fukumura A, et al. Polyethylene as a radiation shielding standard in simulated cosmic-ray environments. Nucl Instr Meth B 2006; 252:319–32.

34. Miller J, Zeitlin C, Cucinotta FA, Heilbronn L, Stephens D, Wilson JW. Benchmark studies of the effectiveness of structural and internal materials as radiation shielding for the international space station. Radiat Res 2003; 159:381–90.

35. Zeitlin C, Heilbronn L, Miller J, Rademacher SE, Borak T, Carter TR, et al. Heavy fragment production cross sections from 1.05 GeV/nucleon 56Fe in C, Al, Cu, Pb, and CH$_2$ targets. Phys Rev C 1997; 56:388–97.

36. Schall I, Schardt D, Geissel H, Irnich H, Kankeleit E, Kraft G, et al. Charge-changing nuclear reactions of relativistic light-ion beams (5 $\leq$ Z $\leq$ 10) passing through thick absorbers. Nucl Instr Meth B 1996; 117:221–34.

37. Zeitlin C, Guetersloh, S, Heilbronn, L, Miller J, Fukumura A, Iwata Y, et al. Fragmentation cross sections of 290 and 400 MeV/nucleon (12)C beams on elemental targets. Phys Rev C 2007; 76:014911.

38. Alpat B, Pilcer E, Blasko S, Caraffini D, Di Capua F, Postolache V, et al. Total and partial fragmentation cross-section of 500 MeV/ nucleon carbon ions on different target materials. IEEE Trans Nucl Sci 2013; 60:4673–82.

39. Kramer M, Scifoni E, Schuy C, Rovituso M, Tinganelli W, Maier A, et al. Helium ions for radiotherapy? Physical and biological verifications of a novel treatment modality. Med Phys 2016; 43:1995–2004.

40. Horst F, Schuy C, Weber U, Brinkmann KT, Zink K. Measurement of charge- and mass-changing cross sections for He 4 + C 12 collisions in the energy range 80–220 MeV/u for applications in ion beam therapy. Phys Rev C 2017; 96:1–11.

41. Newhauser WD, Zhang R. The physics of proton therapy. Phys Med Bio 2015; 60:R155–209.

42. Norbury JW, Schimmerling W, Slaba TC, Azzam EI, Badavi FF, Baiocco G, et al. Galactic cosmic ray simulation at the NASA Space Radiation Laboratory. Life Sci Space Res 2016; 8:38–51.

43. Norbury JW, Miller J, Adamczyk A, Heilbronn LH, Townsend LW, Blattnig SR, et al. Nuclear data for space radiation. Radiat Meas 2012; 47:315–63.

44. Norbury JW, Miller J. Review of nuclear physics experimental data for space radiation. Health Phys 2012; 103:640–2.

45. McGirl NA, Castellanos LA, Srikrishna AP, Heilbronn L, La Tessa C, Rusek A, et al. Accelerator-based measurements relevant for shielding design in space. IEEE Aerospace Conference Proceedings. Big Sky, MT: 2016; 7500858. (https://ieeexplore.ieee.org/document/7500858/)

46. Castellanos LA, McGirl NA, Srikrishna AP, Heilbronn L, Srikrishna AP, La Tessa C, et al. Thick-target yields of secondary ions and neutrons for validation of radiation transport codes. IEEE Aerospace Conference Proceedings. Big Sky, MT: 2017; 7943575. (https://ieeexplore.ieee.org/document/7943575/)